Elsevier Editorial System(tm) for Acta Biomaterialia

Manuscript Draft

Manuscript Number: AB-20-938R2

Title: A full-field 3D Digital Image Correlation and Modelling Technique to Characterise Anterior Cruciate Ligament Mechanics ex vivo

Article Type: Full length article

Keywords: Anterior cruciate ligament; three-dimensional digital image correlation; finite element model; inverse finite element analysis; viscoelastic properties

Corresponding Author: Dr. Rosti Readioff, Ph.D., MEng (Hons)

Corresponding Author's Institution: Keele University

First Author: Rosti Readioff, Ph.D.

Order of Authors: Rosti Readioff, Ph.D.; Brendan Geraghty; Eithne Comerford; Ahmed Elsheikh

Abstract: It is limiting to use conventional methods when characterising material properties of complex biological tissues with inhomogeneous and anisotropic structure, such as the anterior cruciate ligament (ACL) in the knee joint. This study aims to develop and utilise a three-dimensional digital image correlation method (3D DIC) for the purpose of determining material properties of femur-ACL-tibia complex across the surface without any contact between the tissue and the loading equipment. A full-field (360° view) 3D DIC test setup consisting of six digital single-lens reflex cameras was developed and ACL specimens from skeletally mature dog knee joints were tested. The six cameras were arranged into three pairs and the cameras within each pair were positioned with 25^{0} in between to obtain the desired stereovision output. The test setup was calibrated twice: first to obtain the intrinsic and extrinsic parameters within camera pairs, and second to align the 3D surfaces from each camera pair in order to generate the full view of the ACLs. Using the undeformed 3D surfaces of the ligaments, ACL-specific finite element models were generated. Longitudinal deformation of ligaments under tensile loads obtained from the 3D DIC, and this was analysed to serve as input for the inverse finite element analysis. As a result, hyperelastic coefficients from the first-order Ogden model that characterise ACL behaviour were determined with a marginal error of <1.5 %. This test setup and methodology provides a means to accurately determine inhomogeneous and anisotropic material properties of ACL. The methodology described in this study could be adopted to investigate other biological and cultured tissues with complex structure.

Cover Letter

Rosti Readioff, MEng PhD CEng
Postdoctoral Research Associate

Guy Hilton Research Centre,
Keele University
Stoke-on-Trent, UK

March 29th 2020

Dear Professor William Wagner,

We wish to submit an original research article entitled “A Novel Imaging and Modelling Technique to Characterise Anterior Cruciate Ligament Mechanics *ex vivo*” for consideration by Acta Biomaterialia.

We confirm that this work is original and has not been copyrighted, published, submitted, or accepted for publication elsewhere.

In this paper, we report the development and utilisation of a novel and non-conventional methodology involving full-field three-dimensional digital image correlation (3D DIC) and finite element analysis to investigate material properties of biological tissues with complex anatomical structure in a controlled environment. This is significant because, unlike conventional methods where contact measurements are adopted to characterise material properties of soft biological tissues such as anterior cruciate ligament, our novel method is based on non-contact optical measurements where deformation all around and across the surface of the specimen is monitored. Our full-field optical measurement technique reduces inaccuracies due to clamping and more importantly considers the inhomogeneous nature of the specimen. With the aid of 3D DIC and specimen specific inverse finite element analysis, we determined material parameters of the ligaments, which can be adopted in numerical studies of the ligament.

An article on the application of single view DIC by Mallett and Arruda (2017) has been publish in Acta Biomaterialia, and recently another article on the application of DIC to developing devices for residual limbs by Solav *et al.* 2019 in IEEE transactions of biomedical engineering have been published. Both original articles are highly cited which lead us to believe that our paper on 3D DIC and inverse modelling is both timely, and relevant to your journal.

In addition, we believe that this manuscript is appropriate for publication by Acta Biomaterialia and of interest to its readership because it contains engineering development in methods for biomaterial characterisation. With our methodology, researchers can investigate the non-uniform deformation of soft biological tissue, including cruciate ligaments, Achilles tendon and bioengineered tissues.

Thank you for your consideration of this manuscript.

Sincerely,

Rosti Readioff

Statement of Significance

Determining the material properties of soft tissues with complex anatomical structure, such as the anterior cruciate ligament (ACL), is important to better understand their contribution to musculoskeletal biomechanics. Current conventional methods for characterising material properties of the ACL are often limited to a contact measurement approach, however an improved understanding of the mechanics of this complex tissue is vital in terms of preventing injury and developing novel therapies. This article reports the development and utilisation of non-contact optical methodology involving full-field three-dimensional digital image correlation and finite element analysis to accurately investigate material properties of the ACL, in a controlled environment. This technique reduces inaccuracies due to specimen clamping and more importantly considers the inhomogeneous nature of the examined tissue.

A full-field 3D Digital Image Correlation and Modelling Technique to Characterise Anterior Cruciate Ligament Mechanics *ex vivo*

(AB-20-938R1)

RESPONSE TO REVIEWERS' COMMENTS

We thank the Editor and Reviewer for taking the time to read our revised work and provide their helpful and constructive comments. We have addressed the points raised by both the Editor and the Reviewer. The Editor and Reviewer's comments are displayed in italics and our response is given immediately below in plain text. We have also highlighted the corresponding changes in our manuscript (previous revision was highlighted in yellow and the current revision is highlighted in green).

Editorial Office:

1. Please submit a text file containing the figure legends separately from both the figures and the body of the manuscript.

We thank the Editor for their suggestion. We have now created a text file only containing the Figure legends.

2. Please increase the size and legibility of the text in the Graphical Abstract as it will not be readable at the size published online.

We have revised and simplified the Graphical Abstract allowing us to increase the size of the text whilst adhering to the requirements specified by the journal. The maximum font size we have used is 15, and the minimum font size is 13.

Reviewer #1:

3. I congratulate with the Authors with their excellent job in addressing all the comments and in providing exhaustive details.

I sincerely appreciate the value of the paper in its current form.

We thank the Reviewer very much for their comment.

4. As a final remark, please, check the significance of adding the 3-4 significant digits in Tables 1, 2, 3.

For instance:

- Table 1: 2 decimals for mu and alpha would be enough

- Tables 2 and 3: aren't 3 decimals too many for a displacement measurement? Given the percentage values is high, approximating to the first unit (no decimals) would be sufficient.

Table 1: We agree with the Reviewer. We have now reduced the decimal points from three to two for mu and alpha, and their corresponding statistical data.

Table 2 and 3: We have now reduced the decimal points for the coefficient of variations to remove the decimal points. However, we have left the displacement measurements as three decimal points because we were able to capture deformation to five decimal points from our imaging setup. We have also revised and modified the main text of the article to reflect the changes we have made in the Tables 1, 2 and 3. New modifications are highlighted in green.

Modified paragraph in the main text (Lines 332-337):

Variabilities across the specimens showed the highest standard deviation of 54% of the mean and this value decreases with increasing the applied load with the lowest value being 39% (Table 2). Specimen one, two and three showed similar patterns of decreasing coefficient of variation with increasing loads (Table 3). The range of coefficient of variation in specimen five was 22 to 26 %, which is noticeably smaller compared to the rest of the specimens (Table 3).

Modified Tables:

Table 1

Numerical parameters (μ and α) derived from inverse analysis of the ACL-specific finite element models defining non-linear hyperelastic characteristics of the ACLs. Root mean square (RMS) values represents the accuracy achieved between experimental and numerical data during the inverse analysis. There are two suspected outliers, and they are μ for specimen one and α for specimen three. The coefficient of variation for both parameters might have been affected because of the suspected outliers.

Specimen No.	μ	α	RMS (%)
1	2.58	20.36	0. 63
2	0.23	17.72	1.11
3	0.82	70.32	0.53
4	0.64	44.52	0.67
5	0.08	14.31	0.76
First Quartile (25%)	0.16	16.01	
Third Quartile (75%)	1.70	57.42	
Interquartile Range (IQR)	1.54	41.40	
Suspected Outliers (Inner Fence: 1.5 x IQR)	2.32	62.11	
Outlier (Outer Fence: 3 x IQR above third quartile)	6.33	181.63	
Outlier (Outer Fence: 3 x IQR below first quartile)	4.48	108.20	
Mean	0.87	33.44	

Standard Deviation	1.00	23.81
Coefficient of Variation (%)	115.24	71.18
Mean – excluding outlier	0.44	24.23
Standard Deviation – excluding outlier	0.34	13.75
Coefficient of Variation – excluding outlier	78.05	56.77

Table 2

Longitudinal displacement obtained from the digital image correlation test setup, their corresponding standard deviation, and the coefficient of variation values across the five cadaveric specimens. The highest standard deviation is 54% of the mean and this value decreases with increasing the load with the lowest value being 39%.

Load (N)	Longitudinal Displacement (mm)	Standard Deviation	Coefficient of Variation (%)
0.0	0	0	N/A
1.1	0.074	0.040	54
2.2	0.129	0.063	49
3.3	0.168	0.079	47
4.4	0.198	0.088	44
5.5	0.229	0.099	43
6.6	0.257	0.108	41
7.7	0.278	0.112	40
8.8	0.300	0.120	39
9.9	0.318	0.124	39

Table 3

Longitudinal displacement obtained from the digital image correlation test setup, their corresponding standard deviation, and the coefficient of variation values within the specimens. The standard deviation describes variability of data obtained from different camera pairs. Abbreviations: Dis, longitudinal displacement; SD, standard deviation of the mean; CV, coefficient of variation.

Load (N)	Specimen 1			Specimen 2			Specimen 3			Specimen 4			Specimen 5		
	Dis (mm)	SD	CV (%)	Dis (mm)	SD	CV (%)	Dis (mm)	SD	CV (%)	Dis (mm)	SD	CV (%)	Dis (mm)	SD	CV (%)
0.0	0.000	0.000	N/A	0.000	0.000	N/A	0.000	0.000	N/A	0.000	0.000	N/A	0.000	0.000	N/A
1.1	0.028	0.010	36	0.086	0.047	55	0.036	0.025	69	0.116	0.048	41	0.105	0.024	22
2.2	0.061	0.020	32	0.141	0.073	51	0.065	0.043	66	0.193	0.082	42	0.183	0.042	22
3.3	0.085	0.027	32	0.179	0.089	49	0.087	0.058	66	0.246	0.110	44	0.241	0.059	24
4.4	0.110	0.033	30	0.209	0.101	48	0.105	0.069	66	0.279	0.127	45	0.285	0.073	25
5.5	0.134	0.039	29	0.243	0.109	44	0.121	0.080	65	0.312	0.145	46	0.334	0.088	26
6.6	0.158	0.043	26	0.269	0.113	41	0.136	0.089	65	0.341	0.162	47	0.378	0.086	22
7.7	0.178	0.048	27	0.292	0.117	40	0.149	0.098	65	0.364	0.176	48	0.406	0.099	24
8.8	0.197	0.051	25	0.314	0.122	38	0.161	0.105	65	0.387	0.192	49	0.440	0.100	22
9.9	0.214	0.055	25	0.330	0.132	39	0.172	0.110	64	0.409	0.206	50	0.463	0.104	22

*Graphical Abstract

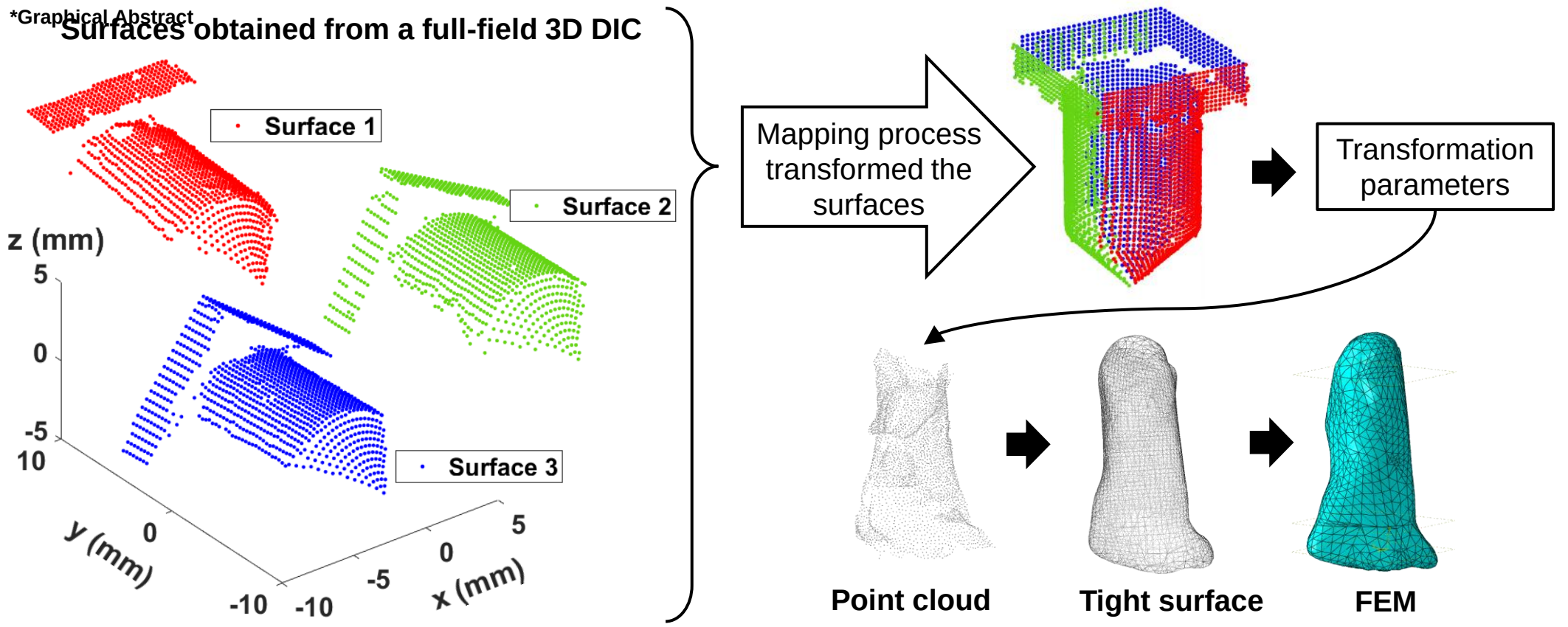

A full-field 3D Digital Image Correlation and Modelling Technique to Characterise Anterior Cruciate Ligament Mechanics *ex vivo*

Rosti Readioff[1*], Brendan Geraghty[2], Eithne Comerford[2, 3] and Ahmed Elsheikh[1, 4, 5]

Affiliations:

[1] School of Engineering, University of Liverpool, Liverpool, L69 3GH, UK

[2] Institute of Life Course and Medical Sciences, University of Liverpool, William Henry Duncan Building, 6 West Derby Street, L7 8TX, UK

[3] Institute of Veterinary Science, Leahurst Campus, University of Liverpool, Chester High road, Neston, CH64 7TE

[4] Beijing Advanced Innovation Center for Biomedical Engineering, Beihang University, Beijing, 100083, China

[5] National Institute for Health Research (NIHR) Biomedical Research Centre at Moorfields Eye Hospital NHS Foundation Trust and UCL Institute of Ophthalmology, UK

*Corresponding Author

Rosti Readioff

r.readioff@keele.ac.uk

Current affiliation: School of Pharmacy and Bioengineering, Keele University, ST4 7QB.

Abstract

It is limiting to use conventional methods when characterising material properties of complex biological tissues with inhomogeneous and anisotropic structure, such as the anterior cruciate ligament (ACL) in the knee joint. This study aims to develop and utilise a three-dimensional digital image correlation method (3D DIC) for the purpose of determining material properties of femur-ACL-tibia complex across the surface without any contact between the tissue and the loading equipment. A full-field (360° view) 3D DIC test setup consisting of six digital single-lens reflex cameras was developed and ACL specimens from skeletally mature dog knee joints were tested. The six cameras were arranged into three pairs and the cameras within each pair were positioned with 25º in between to obtain the desired stereovision output. The test setup was calibrated twice: first to obtain the intrinsic and extrinsic parameters within camera pairs, and second to align the 3D surfaces from each camera pair in order to generate the full view of the ACLs. Using the undeformed 3D surfaces of the ligaments, ACL-specific finite element models were generated. Longitudinal deformation of ligaments under tensile loads obtained from the 3D DIC, and this was analysed to serve as input for the inverse finite element analysis. As a result, hyperelastic coefficients from the first-order Ogden model that characterise ACL behaviour were determined with a marginal error of <1.5 %. This test setup and methodology provides a means to accurately determine inhomogeneous and anisotropic material properties of ACL. The methodology described in this study could be adopted to investigate other biological and cultured tissues with complex structure.

Keywords

Anterior cruciate ligament; three-dimensional digital image correlation; finite element model; inverse finite element analysis; viscoelastic properties.

1. Introduction

Measuring mechanical properties of soft biological tissues such as knee joint ligaments are valuable for biomedical research and developing medical products. Due to the anisotropic, non-linear and inhomogeneous nature of knee ligaments, it is challenging to characterise their mechanical properties using conventional methods.

There are different engineering systems to measure material deformation of such complex tissues, including measuring the deformation by assuming that the strain field is homogenous in the gauge area and the lengthening of the specimen corresponds to the displacement of the machine crosshead [1]. Other systems are based on contact or non-contact measurement techniques [2,3]. A contact measurement technique acts as a single-point gauge or an extensometer, therefore; it can only record strain from one small area. Non-contact measurement techniques using optical approaches such as digital image correlation (DIC) allow local strain measurements to be taken on the surface of an object without any contact between the object and its strain measurement equipment [4,5].

Different arrangements of DIC involving the use of single and multi-camera with two- or three-dimensional capabilities have been described [4,6–11]. A two-dimensional (2D) DIC technique was first utilised in the 1980s [4,5] and consists of a single fixed camera which results in limited measurement of the in-plane (x-y plane) deformation of the object under loading. Any out-of-plane (x-z and y-z planes) deformation changes the magnification and leads to errors in the deformation measurements. Errors due to oblique angle observations, present in the 2D setup, are compensated for in the three-dimensional (3D) DIC method [5,12,13]. As with stereopsis, a 3D DIC setup is based on photogrammetric principles and uses images of the same object from at least two different angles to calculate the 3D coordinates of the entire surface [7,14].

Three-dimensional DIC has been proven to be an accurate and reproducible tool for strain measurements in soft biological tissues because DIC measures the tissue-level strain and it

is not affected by the mechanical measuring system (i.e. test clamps or strain gauge) [15–22]. A study showed that strain values measured using a DIC method was lower than that measured using a traditional grip-to-grip method [19]. This difference was thought to be mainly due to slippage of the tissue within the grip system [23]. 3D DIC also has challenges including those caused by the size and shape of the test specimen when using two-camera systems [24]. For example, an object with complex curvature may produce visual blind spots that the cameras cannot resolve properly into an accurate 3D image. In these cases, a multi-camera 3D DIC system has been reported to overcome the difficulties with monitoring surface strain [24,25].

In order to apply a DIC system to soft biological tissues, such as knee ligaments with little to no texture, a speckle pattern needs to be generated on the area under observation [26]. Researchers used different approaches to create speckle patterns on biological tissues and no study has reported significant changes in the material characteristics of the tissues after the application of paint [15,18,19].

Recently, a framework using multi-view 3D DIC for measuring the time-varying shapes of residual limbs has been reported with an intention to better design wearable technologies [27]. The framework is thought to be useful in characterising soft tissue mechanics. However, considerable modifications including installation of new camera lenses and test rig arrangements are required in order to perform *ex-vivo* mechanical tests on a cadaveric knee ligament in a controlled environment such as hydration. Other studies developed 3D DIC systems to characterise material properties of the Achilles tendon [14], superficial medial collateral ligament [17], and ovine anterior cruciate ligament [19]. It is of critical importance that in determining our understanding of the mechanical properties of the anterior cruciate ligament (ACL) that techniques used do not compromise its inhomogeneous and complex structure. Hence, in this study we developed a methodology to test complex bone-ligament-bone constructs as whole structures. The methodology in this study comprised of developing and utilising a full-field (360° view) multi-camera 3D DIC method with inverse finite element

analysis to derive representative material properties of tissues with complex geometry and structure. A preliminary version of this work has been reported [28].

2. Material and methods

2.1. Specimen Preparation

Five disease-free knee joints (determined to be disease-free by a boarded veterinary orthopaedic specialist using the Outerbridge criteria) from cadavers of skeletally mature Staffordshire bull terrier dogs were obtained with full ethical permission from the institutional veterinary research ethics committee (RETH000553 and VREC65). The dogs were euthanised for reasons other than musculoskeletal injury. Knee joints with bodyweight >20 kg (range: 21.5 to 29.4 kg) and age >18 months (range: 1.8 to 3 years old) were collected for this study. The entire knee joints were frozen at -20°C until required and defrosted at room temperature (20°C) prior to removing the anterior cruciate ligaments (ACL) as a femur-ligament-tibia complex. Storage and refreezing of the ligament is suggested to have little or no effect on the biomechanical properties [29,30].

The five ACLs were extracted with precision to avoid damage to the ligament and ensure that 10 mm of bone was left on each side of the ligament (Fig. 1a and b). The 10mm femur and tibia bone sections that were left connected to the ligament formed a femur-ACL-tibia complex and allowed the measurement of end-to-end ligament deformation as well as helping to facilitate the clamping of the specimen. These dissected specimens were wrapped in paper soaked with phosphate buffered saline (PBS) and frozen at -20 ºC to preserve them until they were required for testing. Before any tests took place, the specimens were thawed in room temperature (20°C). Two 1.1mm arthrodesis wires (Veterinary Instrumentation, Sheffield, UK) were drilled through the tibia and femur bone ends to assist with clamping the ACLs. The ACL turns on itself in a slight proximal-to-distal (lateral) outward spiral and this

spiral feature has been reported to be approximately 90 degrees [31,32]. The ACLs were clamped such that this spiral feature was replicated when mounted in the test setup.

2.2. Full-Field 3D DIC Setup

The ACLs were secured using a custom-built stainless-steel clamp to an Instron 3366 tensile testing machine fitted with a 10 N load-cell (Instron, Part No. 2530-428). The ACLs were sprayed with fast drying matt black colour paint (RS 764-3039 – based on alkyd resins and insoluble in water) to create randomly distributed and distinct speckles with an optimal speckle size of 0.02 – 0.2 mm (Fig. 1c) [18]. A preload of 0.1 N was applied to remove laxity within the ACL and the ACLs were preconditioned by performing five loading-unloading cycles to a maximum load of 9.9 N at strain rate of 10 %/min. The ACLs were then tested to determine their tensile behaviour at 1 %/min strain rate up to a maximum load of 9.9N and this range was chosen to observe the viscoelastic behaviour of the ligament [33]. Deformation images were taken at 1.1 N intervals during loading using the full-field 3D DIC setup [24,26]. A multi-camera trigger box, built in-house, was used to visually synchronise the applied loads with the images. Specimen deformation was monitored in three directions (x, y, and z), using six digital single-lens reflex (DSLR) camera bodies with Canon EF 100mm f2.8 USM Macro lenses (Canon, Tokyo, Japan), obtaining 5184 x 3456 pixels per image. Adjacent cameras were paired generating three camera pairs in total and the cameras within each pair were positioned with 25º in between to obtain the desired stereovision output. The first pair consisted of cameras 1 and 2, the second pair cameras 3 and 4 and the third pair cameras 5 and 6 (Fig. 2a and b). As shown in Fig. 2a, front (detachable) and back (stationary) frames were custom designed around the materials testing machine in order to hold the cameras in place around the ACL on the load cell. The centreline of the first pair was positioned at 130º to both the second and third pairs whilst the centrelines of the second and third pairs were positioned at 100º to one another. This positioning of camera pairs facilitated a full field (360º view) of the ACL (Fig. 2b).

During mechanical tests, the ACL was kept in a custom-made stainless-steel tank accommodating the cameras around the specimen and controlling specimen hydration and degradation using 20ml buffer solution (15ml of 20mM Tris pH 7.5, 150 mM NaCl, 5 mM $CaCl_2$) with protease inhibitors (1 tablet of mini-cOmplete per 10 ml of buffer, SIGMA-ALDRICH/Roche, USA) [34]. This custom-made tank was built by creating a 3D model of the required tank using AutoCAD 3D (AutoCAD 2014, Autodesk, US) and then the tank was manufactured based on this customised design. The body of the tank was made of stainless-steel to avoid any potential chemical reactions or contamination between the tank and its medium. Six windows were introduced into the steel tank to accommodate views of the ACL (Supplementary Materials Fig. S1). These windows, made from 3mm thick borosilicate glass pieces (Spectraglass Ltd, Perth, UK), were positioned orthogonally (90° ± 0.1°) to the cameras minimising the distortion due to light refraction, especially when light passed between the different media (i.e. between the air and the glass windows and between the glass windows and the buffer solution) [18].

The multi-camera 3D DIC system was calibrated twice; firstly, for determining the image parameters (intrinsic and extrinsic parameters) within the paired cameras (for instance, calibrating camera 1 with 2, camera 3 with 4, and camera 5 with 6) and secondly between each camera pair (for instance, calibrating the position of camera pair 1 with pair 2 and pair 3).

2.2.1. Calibration I: Calibration of the cameras

In the first calibration process, the intrinsic and extrinsic parameters between two adjacent cameras (projection parameters) were obtained. To describe briefly, the intrinsic parameters are internal and fixed to a camera and allow a mapping between camera coordinates and pixel coordinates in the image frame. The extrinsic camera parameters, the relative position and orientation of one camera relative to another, are external to the camera. These projection parameters were obtained by firstly taking images of a Dantec Dynamic's calibration plate (Dantec Dynamics 1.5mm 9x9 marked white glass calibration target, Dantec

Dynamics, Denmark, 2014). The calibration plate was immersed inside the test solution within the steel tank in order to calibrate the cameras to the environment where the ACL would be tested. Images of the calibration plate were taken by one camera pair at a time and these images were analysed using Istra4D software (Dantec Dynamics, Denmark, 2014) to calculate the projection parameters for all three camera pairs. The software also estimated a mean residual deviation (deviation between synthetic and real-world images) indicating an average uncertainty of the detected markers on the target plate. In this study, a mean residual deviation of less than 1 pixel was achieved indicating a reliable calibration process as suggested by the software manual.

2.2.2. Calibration II: Calibration of the DIC setup

The second calibration process was performed to ensure the three 3D topographies created from each camera pair would successfully reproduce a full (360°) view of the tested ACLs. This calibration involved capturing one image of a rotationally non-symmetric rigid object with a known geometry by all three camera pairs (Supplementary Materials Fig. S2). This reference object was custom-built out of steel with a high manufacturing resolution (±0.05 mm). The surface of the reference object was painted in matt white to give a distinct bright surface and then spray painted in matt black to create speckle patterns on the white surface. This object was placed in the same environment and position as the ACLs would be positioned during tensile tests. Subsequently, these images were analysed using Istra4D software in order to extract x, y and z coordinates representing the three surfaces of the reference object captured by the three camera pairs. To achieve optimal accuracy in DIC image analysis, a minimum of three speckles per facet and grid size (defining the distance between the centres of the facets) equal to 2/3rd of the facet size were applied [26]. After solving the facets from the images, three sets of data (x, y and z coordinates) representing 3D surfaces were obtained from each camera pairs.

2.3. DIC Image Analysis of the ACLs

One image of each ACL was taken from all six cameras after preloading the ligament and, subsequently, multiple images were taken at different load points. Images captured after preloading the ligament were used to construct three surfaces in 3D, whereas the successive images of the ligament during tensile tests were used to obtain load-deformation plots. Due to the complex anatomical structure of the ACL, in particular the proximal-to-distal outward spiral in the ACL, there were minor (approximately <8% of total area) blind spots where the cameras could not capture the speckle pattern (Supplementary Materials Fig. S3). Hence, there were regions across the surface of the ACL, such as the tibial and femoral insertion areas, with missing data points and these regions were recreated using Poisson's surface reconstruction through MeshLab (MeshLab, Visual Computing Lab – Italian National Research Council - CNR, Italy) [35,36].

In this study, three load-deformation plots at the middle region of the ACLs were generated for each camera pair.

2.4. Generation of ACL 3D Geometry

The 3D geometry of ACL was generated by aligning the surfaces from the three camera pairs. Transformation parameters were utilised to align the 3D ACL surfaces, and these parameters were obtained from the images of the rotationally non-symmetric rigid object (reference object) as stated in Calibration II.

To obtain the transformation parameters from the reference object, the three surfaces of the object in 3D were aligned and combined using iterative registrations [37]. Initially, the coordinate transformation (rotation (R), and translation (t)) that matched two surfaces of the reference object, static surface S and dynamic surface D, were found. Each surface was defined by discrete sets of data points ($s_i \epsilon S; i = 1, 2, 3, \dots, n$) and ($d_j \epsilon D; j = 1, 2, 3, \dots, m$). The static surface S was generated by inputting the exact dimensions of the calibration

object using MATLAB, whilst the dynamic surface D was the data collected from the three camera pairs using the 3D DIC setup. The dynamic surface D underwent an extrinsic rotation R and translation t about the origin of the fixed coordinate system of the static surface S, as in (1). These translation and rotation parameters, as shown in equations (2) and (3), were necessary to perform the surface matching process.

$$\bar{d}_j = Rd_j + t \tag{1}$$

where the overbar represents the transformed data points in terms of x, y, and z coordinates, and all data points $j = 1, 2, 3, \dots, m$ are required to undergo the same transformation. The rotation matrix is given by

$$R = R_x R_y R_z \tag{2}$$

where

$$R_x = \begin{bmatrix} 1 & 0 & 0 \\ 0 & cos\,\theta_x & -sin\,\theta_x \\ 0 & sin\,\theta_x & cos\,\theta_x \end{bmatrix}$$

$$R_y = \begin{bmatrix} cos\,\theta_y & 0 & sin\,\theta_y \\ 0 & 1 & 0 \\ -sin\,\theta_y & 0 & cos\,\theta_y \end{bmatrix}$$

$$R_z = \begin{bmatrix} cos\,\theta_z & -sin\,\theta_z & 0 \\ sin\,\theta_z & cos\,\theta_z & 0 \\ 0 & 0 & 1 \end{bmatrix}$$

$\theta_x, \theta_y, and\ \theta_z$ are Euler angles

$$t = (t_x t_y t_z)^T \quad (3)$$

where T denotes matrix transposition.

The process of registration focused on determining transformation (rotation and translation) parameters ($t_x, t_y, t_z, \theta_x, \theta_y, and\ \theta_z$). Once these parameters were found, the topography of the dynamic surface overlapped the topography of the static surface. These transformation parameters were estimated using the point-to-point Iterative Closest Point algorithm on both static and dynamic surfaces [38]. The accuracy of this matching process was assessed based on root mean square values (RMS) as a percentage (4). In this study 100 iterations were selected to calculate the optimal match between the two surfaces based on the satisfactory value achieved for the RMS.

$$RMS = \frac{1}{L} \times \sum_{l=1}^{L} \sqrt{\left(\frac{1}{K}\right) \sum_{k=1}^{K} (S_k - D_k)^2} \times 100 \quad (4)$$

where L is the total number of dynamic surfaces obtained from the cameras (L=3), K is the number of surface points, S_k and D_k are $3 \times n$ matrices defining the static and dynamic surfaces.

Once the satisfactory transformation parameters were obtained, they were then used on the three separate surfaces of the ACLs to create a combined 3D surface. The post-processing

operation to create an error-free volumetric computer model of the ACL comprised of refining the mesh surface using Poisson surface reconstruction algorithm [39], computing normal vectors of coordinate points and Poisson-disk sampling [40] using MeshLab and MIMICS (Materialise, Leuven, Belgium).

2.5. Generation of ACL Finite Element Model

The volumetric computer model generated from the 3D geometry of the ACL was converted into a finite element model using ABAQUS finite element modelling software (ABAQUS/Standard 6.13, Dassault Systèmes Simulia Corp., Rhode Island, USA). The finite element model consisted of hybrid ten-node tetrahedral elements (approximate element global size of <1mm^3) [41] and partitioned into three regions, namely femur, tibia and middle regions. The two regions representing femur and tibia bones were defined as linear elastic materials with elastic modulus and Poisson's ratio of 11 GPa and 0.3 respectively [42,43]. A parametric study investigating the effect of material properties of the bones on the results of the middle region of the ACLs was carried out, and the results confirmed that the material properties of the bones were independent from the results reported on the middle region of the ACLs in this paper (Supplementary Materials Table S1 and S2). The middle region of the ACL model was defined with an isotropic Ogden material model [44] to represent the incompressible and hyperelastic behaviour of the ligament [45–49]. The Ogden form of the strain energy potential for incompressible models is expressed in terms of the principal stretches (5):

$$U = \sum_{i=1}^{N} \frac{2\mu_i}{\alpha_i^2}\left(\bar{\lambda}_1^{\alpha_i} + \bar{\lambda}_2^{\alpha_i} + \bar{\lambda}_3^{\alpha_i} - 3\right) + \sum_{i=1}^{N} \frac{1}{D_i}(J_{el} - 1)^{2i} \quad (5)$$

where U is the strain energy potential, $\bar{\lambda}_i$ is a product of the total volume strain J and the principal stretch λ_i, which is defined as $\bar{\lambda}_i = J^{-\frac{1}{3}}\lambda_i$. μ_i, α_i and D_i are material constants, and D_i values define the compressibility of the material which are chosen as zeros in this study to account for the nearly incompressible nature of the ACLs [50,51]. For the boundary conditions, the tibia region was defined as pinned and the femur region as longitudinally loaded. These boundary conditions were applied throughout-the-thickness of the specimens rather than only at the external surface.

2.6. Inverse Finite Element Analysis of the ACLs

The ACL finite element model was utilised to predict the material parameters μ_i and α_i through an inverse analysis study based on the experimental data for the middle region of the ACL. Particle swarm optimisation, written in MATLAB in combination with ABAQUS, was used in the inverse analysis study to find the optimal material parameters that lead to the best fit between the output from the numerical model and the experimental data, e.g. load-deformation plot [45,52,53]. The optimisation tool was monitoring the minimisation process of RMS values between the experimental and numerical displacement at a central point on the middle region of the ACL. The RMS was calculated as percentages of the final deformation at a particular point across the surface of the ACL (Equation 7) and RMS < 0.1 % was set as a target in this study [18].

$$RMS = \frac{\sqrt{((\frac{1}{N})\sum_{n=1}^{N}(\delta_n^{exp} - \delta_n^{num})^2)}}{\delta_{max,n}^{exp}} \times 100 \quad (6)$$

where N = 10 is the number of load increments, and δ_n^{exp} and δ_n^{num} are the experimental (exp) and numerical (num) deformations at a given point across the surface of the ACL at a particular load point.

2.7. Statistical Analysis

The longitudinal displacement values of the ACLs obtained from the DIC test setup were analysed for their variability across and within the five ACLs. The variabilities across the ligaments were studied by calculating the standard deviation of the mean and the coefficient of variation at different load points. Similarly, standard deviation and coefficient of variation values were calculated for the study of variabilities within the ACLs. For the within specimen study, data from the three camera pairs were used. For example, camera pair one produced a load-displacement curve, and this curve was then compared to the load-displacement curves from camera pairs two and three. In addition, the first and third quartiles were calculated for the hyperelastic material parameters obtained from the inverse finite element analysis. The interquartile range calculated from the first and third quartiles was used to identify outliers, with suspected outliers being defined as any value greater than or equal to 1.5 times the range.

3. Results

3.1. Full-Field 3D DIC

The load-displacement plots obtained from the correlation of successive images during tensile testing presented non-linear behaviour which was similar to the findings from the Instron testing machine (Fig. 3). The load-displacement curves of a region farthest away from the moving crosshead of the testing machine (i.e. lower region) extended the least compared to the middle region and top region. For example, at 5.5 N load, longitudinal displacement values for the lower, middle, and top regions were 0.11, 0.23, and 0.36 mm

respectively. The longitudinal displacement value recorded from the Instron testing machine at 5.5 N was 0.49 mm. In addition, the total displacement (resultant value of displacement in three dimensions) across the surface of the ligament showed that the lower region of the ACLs extended less than regions closer to the test crosshead (Fig. 4). This finding was similar to the characteristics observed in Fig. 3. The total displacement and longitudinal true strain across the surface of the ligament, in particular the middle region, was non-uniformly distributed (Fig. 4).

It should be noted that the speckle patterns, produced from the water insoluble paint, adhered to the surface of the ligament throughout the mechanical test. The adherence of the paint on the ligament was not noticeably affected by the buffer solution used for controlling specimen hydration.

The experimental load-displacement curves showed variabilities across and within the five ACLs. Variabilities across the specimens showed the highest standard deviation of 54% of the mean and this value decreases with increasing the applied load with the lowest value being 39% (Table 2). Specimen one, two and three showed similar patterns of decreasing coefficient of variation with increasing loads (Table 3). The range of coefficient of variation in specimen five was 22 to 26 %, which is noticeably smaller compared to the rest of the specimens (Table 3).

3.2. ACL Finite Element Model

To generate an ACL-specific finite element model, a surface matching process (iterative closest point method) was undertaken to obtain transformation parameters for the 3D DIC setup. The transformation parameters for each surface changed with more iterations and optimal values with RMS <0.24 % were achieved after 30 iterations (Supplementary Materials Fig. S5). Once the transformation parameters were obtained, they were utilised in the generation of five ACL-specific finite element models (Fig. 5). These ACL models

consisted of three parts, separating the middle region of the ACLs with tibia and femur bones at each end. Both tibia and femur bones were used as boundary conditions.

3.3. Inverse Finite Element Analysis of the ACLs

Parameters for the ACL-specific finite element models were derived through the inverse analysis process to simultaneously represent characteristics of a hyperelastic material model (Table 1). Variabilities were noticed across the specimens, the standard deviations were 78.05% and 56.77% of the mean values for μ and α, respectively. With the aid of ABAQUS software, nominal stress and strain values were calculated so that they can be compared with results from relevant literature [19,33,55] (Supplementary Materials Table S3 and S4). As shown in Fig. 7, the median values of nominal stress fall within the range of stress values reported in the previous studies. The stress values reported in Mallett and Arruda [19], however, were several magnitudes higher than the previous literature. We suspect that this is because Mallett and Arruda tested on ovine ACLs and they separated the anterior and posterior bundles of the ligament for their tensile tests, whereas similar to the current study, both studies reported in Fig. 7 used dog ACLs as their femur-ligament-tibia complex model.

The particle swarm optimisation utilised in the inverse analysis showed RMS values reducing to <1.5 % by the 50th iteration (Supplementary Materials Fig. S6).

Stress and logarithmic strain distribution across the surface of an ACL-specific finite element model is shown in Fig. 6. For this specimen, the highest stress and strain values were observed around the inward middle structure of the ligaments, with stress values ranging from 0.6 to 0.75 MPa and logarithmic strain ranging from 0.064 to 0.08 mm/mm. Similar characteristics were observed in the other four ligament specimens (Supplementary Materials Fig. S7).

4. Discussion

In this study we developed a non-conventional technique combining 3D imaging and numerical modelling methods to characterise material behaviour of intact anterior cruciate ligaments. The imaging technique comprised a test setup with six cameras around an Instron tensile test machine to capture full view of tested specimens. The cameras were paired to generate 3D images of the specimens during testing. These images were employed in the creation of ACL-specific finite element models that simultaneously represent material characteristics of the ligaments.

Conventional methods to characterise material properties of complex tissues such as anterior cruciate ligaments (ACLs) underestimate the inhomogeneous and anisotropic structure of ligaments [32,56]. The inhomogeneity of cruciate ligaments comes from their complex macro, micro and ultra-histologic structure [57]. In ACLs, the ligament structure is fibrocartilaginous in composition at the tibial ligament insertion region [56]. Regional variations are impacted by mechanical roles of the ligament, such that regions of ligaments under compressive forces are likely to increase fibrocartilaginous matrix composition, hence creating an inhomogeneous tissue structure [58]. In addition, the geometrical structure of anterior cruciate ligaments is complex and non-uniform, making conventional testing method less desirable [59]. Several studies followed the double-bundle model of anterior cruciate ligament anatomy (anterior medial and posterior lateral bundles) and determined material properties of the two bundles by separating one from the other [19,60–62]. This approach may have reduced some of the limitations of conventional mechanical tests by eliminating some of the complexity of the ligament structure and providing a more uniform geometry. However, sectioning the bundles could result in damage to collagen fibres on the ligament surface and result in errors in the material characterisation. Our study tested the ACL as one structure, where potential damage to the tissue surface was prevented, hence structural integrity of the tissue was maintained [63]. Measurement as one structure was possible

through the application of 3D DIC, which allowed us to monitor load distribution across the whole structure of the ligament.

In order to facilitate the 3D DIC analysis, a speckle pattern was applied to the specimen surface. To achieve a good quality of speckle pattern, an optimal speckle size of 0.02 - 0.2 mm randomly spread across the length of the ligament were attained. Studies reported the use of surface markers to measure the gauge length of specimens during testing [64,65] and some researchers optically tracked grip slippage with marks at the tissue-grip interface [66]. However, these studies employed a limited number of markers (ranging from 9-15 per specimen) along the direction of loads which did not provide the high-resolution 3D DIC offers and could not fully assess heterogeneity of the tissue.

In this study, tensile load was applied at a slow strain rate of 1 %/min while images were taken using the 3D DIC setup. Slow strain rate of <10 %/min was selected to investigate the toe region of the stress-strain behaviour of the ACL [3,33,67]. In addition, by applying a tensile load at a slow strain rate, distortion of the deformation images captured from the DSLR cameras was minimised.

The micro lenses on the cameras and the tensile load cell were exceedingly sensitive to vibrations, and care was taken to reduce movements during the experiments. The data collected from the DIC analysis for the longitudinal displacement at the top region of the ligament was lower than data from the materials testing machine which is similar to the previous findings [19]. In this study, surface deformation (longitudinal extension) and strain showed inhomogeneous characteristics across the surface of the ligament and this was also observed in the ACL-specific finite element models. It is important to note that the results showed variations within and across specimens which could be due to varying cadaver demographics, such as age, gender and bodyweight [68].

One of the objectives for the development of our 3D DIC method was to generate specimen specific results. Here, we have generated five ACL-specific finite element models that

simultaneously represent characteristics of the ligaments. The ACL-specific models were subjective in their characteristics; however, similar inhomogeneous trends were observed across the surface of the models (Supplementary Materials Fig. S7).

3D DIC data only from the middle region of the ligament served as input for the optimisation routine to derive constitutive coefficients that characterise ligament behaviour and this is where ACLs undergo uniaxial loading and are susceptible to rupture [19,69]. However, studies using 3D DIC to characterise the human Achilles tendon and ovine anterior medial bundle of anterior cruciate ligament reported that measurements were more accurate at the centre of the specimen, with specimens being relatively homogenous, compared to other regions [17,19]. Due to the complex anatomical structure of the ACL, in particular the proximal-to-distal outward spiral in the ligament, there were some blind spots where the cameras could not track the speckle pattern. We minimised the errors due to this limitation by using the 2D images to aid Poisson surface reconstruction algorithm and reproduce the missing regions.

One of the limitations in this study was the assumption of using an isotropic constitutive model to represent the ACL material properties, however, the ACL inherits an anisotropic characteristic. Therefore, future studies should aim to model the ligament with anisotropic properties. In addition, the current study focused on an overall characterisation in the middle region of the ligament, and this approach excluded other areas of the bone-ligament-bone complex such as the origin and insertion regions of the ligament. One way to overcome this for future studies is to map the correlated facets from the DIC on top of the finite element models of the ACLs in order to create a point-wise resolution of the material properties. The limited number of cadaveric specimens made it challenging to perform descriptive statistical analysis. The variability in results were calculated assuming the normal distribution of data. Finally, although a rigorous and reliable protocol was followed to ensure that the surface displacements were accurately determined during the uniaxial experiments [18,45,53], the inverse analysis procedure has not been validated against a known material. Therefore,

some discrepancies may exist between the optimised material parameters and the intrinsic behaviour of the tissue. However, the maximum RMS errors between the experimental and numerical displacements were between 0.53% to 1.1%, hence these discrepancies are expected to be minimal (Fig. 7).

5. Conclusions

In this study, we developed a methodology to overcome the challenges that are present with utilising conventional mechanical testing to determine material properties of complex biological tissues, such as anterior cruciate ligaments. In this paper, the development and adoption of our methodology which is a combination of full-field 3D DIC and inverse finite element analysis has been demonstrated. The importance of our methodology lies in its ability to capture deformation around the whole structure (360° view) of the ACLs and this information are used as input in the inverse finite element analysis to derive material behaviour across the surface of the ligament.

Conflict of interest statement

None.

Acknowledgment

This work was supported by School of Engineering at the University of Liverpool, a veterinary clinical leave research fellowship from the University of Liverpool Wellcome Trust Institutional Strategic Support Fund (ISSF), and by the National Institute for Health Research (NIHR) Biomedical Research Centre based at Moorfields Eye Hospital NHS Foundation Trust and UCL Institute of Ophthalmology. We thank Mr. Lee Moore, Mr. Ben Jones and the staff at Veterinary Teaching Suite, School of Veterinary Science for their assistance during

sample collection. We also thank Dr Rob Birch and Mr. Ashkan Eliasy at School of Engineering, University of Liverpool, for their assistance during manufacturing parts of the setup.

References

[1] B. Geraghty, S.W. Jones, P. Rama, R. Akhtar, A. Elsheikh, Age-related variations in the biomechanical properties of human sclera, J. Mech. Behav. Biomed. Mater. 16 (2012) 181–191. https://doi.org/10.1016/j.jmbbm.2012.10.011.

[2] H. Ashrafi, M. Shariyat, A Nano-indentation identification technique for viscoelastic constitutive characteristics of periodontal ligaments, J. Biomed. Phys. Eng. 6 (2016) 109–118.

[3] A. Karunaratne, S. Li, A.M.J. Bull, Nano-scale mechanisms explain the stiffening and strengthening of ligament tissue with increasing strain rate, Sci. Rep. (2018). https://doi.org/10.1038/s41598-018-21786-z.

[4] W.H. Peters, W.F. Ranson, Digital imaging techniques in experimental stress-analysis, Opt. Eng. 21 (1982) 427–431. https://doi.org/10.1117/12.7972925.

[5] M.A. Sutton, J. Orteu, H.W. Schreier, Image correlation for shape, motion and deformation measurements: Basic concepts, theory and applications, (2009).

[6] D. Zhang, C.D. Eggleton, D.D. Arola, Evaluating the mechanical behavior of arterial tissue using digital image correlation, Exp. Mech. 42 (2002) 409–416. https://doi.org/10.1007/BF02412146.

[7] M.N. Helfrick, C. Niezrecki, P. Avitabile, T. Schmidt, 3D digital image correlation methods for full-field vibration measurement, Mech. Syst. Signal Process. 25 (2011) 917–927. https://doi.org/10.1016/j.ymssp.2010.08.013.

[8] J. Gao, W. Xu, J. Geng, 3D shape reconstruction of teeth by shadow speckle correlation method, Opt. Lasers Eng. 44 (2006) 455–465. https://doi.org/10.1016/j.optlaseng.2005.04.013.

[9] M.L. Ruspi, M. Palanca, L. Cristofolini, C. Liebsch, T. Villa, M. Brayda-Bruno, F. Galbusera, H.-J. Wilke, L. La Barbera, Digital image correlation (DIC) assessment of the non-Linear response of the anterior longitudinal ligament of the spine during flexion and extension, Mater. Basel Switz. 13 (2020). https://doi.org/10.3390/ma13020384.

[10] M. Palanca, M.L. Ruspi, L. Cristofolini, C. Liebsch, T. Villa, M. Brayda-Bruno, F. Galbusera, H.-J. Wilke, L. La Barbera, The strain distribution in the lumbar anterior longitudinal ligament is affected by the loading condition and bony features: An in vitro full-field analysis, PloS One. 15 (2020) e0227210. https://doi.org/10.1371/journal.pone.0227210.

[11] J. Gardiner, Computational modeling of ligament mechanics, The University of Utah, 2002. https://mrl.sci.utah.edu/papers/Gardiner_dissertation_FINAL.pdf.

[12] Z.X. Hu, H.M. Xie, J.A. Lu, T. Hua, J.G. Zhu, Study of the performance of different subpixel image correlation methods in 3D digital image correlation, Appl. Opt. 49 (2010) 4044–4051. https://doi.org/ 10.1364/Ao.49.004044.

[13] Z.X. Hu, H.M. Xie, J. Lu, H.X. Wang, J.G. Zhu, Error evaluation technique for three-dimensional digital image correlation, Appl. Opt. 50 (2011) 6239–6247. https://doi.org/ 10.1364/Ao.50.006239.

[14] T. Luyckx, M. Verstraete, K. De Roo, W. De Waele, J. Bellemans, J. Victor, Digital image correlation as a tool for three-dimensional strain analysis in human tendon tissue, J. Exp. Orthop. 1 (2014) 1–7.

[15] G. Lionello, C. Sirieix, M. Baleani, An effective procedure to create a speckle pattern on biological soft tissue for digital image correlation measurements, J. Mech. Behav. Biomed. Mater. 39 (2014) 1–8. https://doi.org/10.1016/j.jmbbm.2014.07.007.

[16] T. Luyckx, M. Verstraete, K. De Roo, W. De Waele, J. Bellemans, J. Victor, Digital image correlation as a tool for three-dimensional strain analysis in human tendon tissue, J. Exp. Orthop. 1 (2014) 1–7.

[17] T. Luyckx, M. Verstraete, K. Roo, C. Van Der Straeten, J. Victor, High strains near femoral insertion site of the superficial medial collateral ligament of the knee can

explain the clinical failure pattern, J. Orthop. Res. 34 (2016) 2016–2024. https://doi.org/10.1002/jor.23226.

[18] C. Whitford, A. Joda, S. Jones, F. Bao, P. Rama, A. Elsheikh, Ex vivo testing of intact eye globes under inflation conditions to determine regional variation of mechanical stiffness, Eye Vis. 10 (2016) 3–21. https://doi.org/10.1186/s40662-016-0052-8.

[19] K.F. Mallett, E.M. Arruda, Digital image correlation-aided mechanical characterization of the anteromedial and posterolateral bundles of the anterior cruciate ligament, Acta Biomater. 56 (2017) 44–57.

[20] D. Spera, K. Genovese, A. Voloshin, Application of stereo-digital image correlation to full-field 3-D deformation measurement of intervertebral disc, Strain. 47 (2011) E572–E587. https://doi.org/10.1111/j.1475-1305.2009.00658.x.

[21] K. Genovese, Y.-U. Lee, A.Y. Lee, J.D. Humphrey, An improved panoramic digital image correlation method for vascular strain analysis and material characterization, J. Mech. Behav. Biomed. Mater. 27 (2013) 132–142. https://doi.org/10.1016/j.jmbbm.2012.11.015.

[22] Z. Gao, J.P. Desai, Estimating zero-strain states of very soft tissue under gravity loading using digital image correlation, Med. Image Anal. 14 (2010) 126–137. https://doi.org/10.1016/j.media.2009.11.002.

[23] S. Rigozzi, R. Muller, J.G. Snedeker, Local strain measurement reveals a varied regional dependence of tensile tendon mechanics on glycosaminoglycan content, J. Biomech. 42 (2009) 1547–1552. https://doi.org/10.1016/j.jbiomech.2009.03.031.

[24] F.X. Chen, X. Chen, X. Xie, X. Feng, L.X. Yang, Full-field 3D measurement using multi-camera digital image correlation system, Opt. Lasers Eng. 51 (2013) 1044–1052. https://doi.org/10.1016/j.optlaseng.2013.03.001.

[25] D. Solav, K. M. Moerman, A. M. Jaeger, K. Genovese, H. M. Herr, MultiDIC: An open-source toolbox for multi-view 3D digital image correlation, IEEE Access. 6 (2018) 30520–30535. https://doi.org/10.1109/ACCESS.2018.2843725.

[26] M.A. Sutton, J. Orteu, H.W. Schreier, Image correlation for shape, motion and deformation measurements: Basic concepts, theory and applications, Springer, New York, 2009.

[27] D. Solav, K. M. Moerman, A. M. Jaeger, H. M. Herr, A framework for measuring the time-varying shape and full-field deformation of residual limbs using 3-D digital image correlation, IEEE Trans. Biomed. Eng. 66 (2019) 2740–2752. https://doi.org/10.1109/TBME.2019.2895283.

[28] R. Readioff, B. Geraghty, E.J. Comerford, A. Elsheikh, A novel imaging and modelling technique to characterise ligament mechanics, in: London, 2019: p. 130.

[29] S.L.Y. Woo, C.A. Orlando, J.F. Camp, W.H. Akeson, Effects of postmortem storage by freezing on ligament tensile behavior, J. Biomech. 19 (1986) 399–404. https://doi.org/10.1016/0021-9290(86)90016-3.

[30] D.K. Moon, S.L.Y. Woo, Y. Takakura, M.T. Gabriel, S.D. Abramowitch, The effects of refreezing on the viscoelastic and tensile properties of ligaments, J. Biomech. 39 (2006) 1153–1157. https://doi.org/10.1016/j.jbiomech.2005.02.012.

[31] S.P. Arnoczky, J.L. Marshall, The cruciate ligaments of the canine stifle: An anatomical and functional analysis, Am. J. Vet. Res. 38 (1977) 1807–1814.

[32] S.P. Arnoczky, Anatomy of the anterior cruciate ligament, Clin. Orthop. (1983) 19–25.

[33] R.C. Haut, R.W. Little, Rheological properties of canine anterior cruciate ligaments, J. Biomech. 2 (1969) 289–298. https://doi.org/10.1016/0021-9290(69)90085-2.

[34] T.J. Lujan, C.J. Underwood, N.T. Jacobs, J.A. Weiss, Contribution of glycosaminoglycans to viscoelastic tensile behavior of human ligament, J. Appl. Physiol. 106 (2009) 423–431. https://doi.org/10.1152/japplphysiol.90748.2008.

[35] W. Hou, Z. Xu, N. Qin, D. Xiong, M. Ding, Surface reconstruction through poisson disk sampling, PloS One. 10 (2015) e0120151–e0120151. https://doi.org/10.1371/journal.pone.0120151.

[36] P. Cignoni, M. Callieri, M. Corsini, M. Dellepiane, F. Ganovelli, G. Ranzuglia, Meshlab: an open-source mesh processing tool, Proc. Eurographics Ital. Chapter Conf. (2008) 129–136.

[37] J. Wang, A. Elsheikh, P.G. Davey, W. Wang, F. Bao, J.E. Mottershead, Corneal topography matching by iterative registration, Proc. Inst. Mech. Eng. [H]. 228 (2014) 1154–1167. https://doi.org/10.1177/0954411914559080.

[38] H.M. Kjer, J. Wilm, Evaluation of surface registration algorithms for PET motion correction, 2010.

[39] M. Kazhdan, M. Bolitho, H. Hoppe, Poisson surface reconstruction, Eurographics Symp. Geom. Process. 7 (2006).

[40] M. Corsini, P. Cignoni, R. Scopigno, Efficient and flexible sampling with blue noise properties of triangular meshes, IEEE Trans. Vis. Comput. Graph. 18 (2012) 914–924. https://doi.org/10.1109/Tvcg.2012.34.

[41] A. Elsheikh, C. Whitford, R. Hamarashid, W. Kassem, A. Joda, P. Buchler, Stress free configuration of the human eye, Med. Eng. Phys. 35 (2013) 211–216. https://doi.org/10.1016/j.medengphy.2012.09.006.

[42] D.T. Reilly, A.H. Burstein, V.H. Frankel, The elastic modulus for bone, J. Biomech. 7 (1974) 271–275.

[43] D.T. Reilly, A.H. Burstein, The elastic and ultimate properties of compact bone tissue, J. Biomech. 8 (1975) 393–405.

[44] R.W. Ogden, Non-linear elastic deformations, Ellis Horwood, Chichester, 1984.

[45] C. Whitford, H. Studer, C. Boote, K.M. Meek, A. Elsheikh, Biomechanical model of the human cornea: considering shear stiffness and regional variation of collagen anisotropy and density, J Mech Behav Biomed Mater. 42 (2015) 76–87. https://doi.org/10.1016/j.jmbbm.2014.11.006.

[46] G.A. Holzapfel, R.W. Ogden, Constitutive modelling of arteries, Proc. R. Soc. Math. Phys. Eng. Sci. 466 (2010) 1551–1597. https://doi.org/10.1098/rspa.2010.0058.

[47] Y. Matsuura, A.R. Thoreson, C. Zhao, P.C. Amadio, K.-N. An, Development of a hyperelastic material model of subsynovial connective tissue using finite element modeling, J. Biomech. 49 (2016) 119–122. https://doi.org/10.1016/j.jbiomech.2015.09.048.

[48] K.-J. Chen, A. Eliasy, R. Vinciguerra, A. Abass, B.T. Lopes, P. Vinciguerra, R.J. Ambrósio, C.J. Roberts, A. Elsheikh, Development and validation of a new intraocular pressure estimate for patients with soft corneas, J. Cataract Refract. Surg. 45 (2019) 1316–1323. https://doi.org/10.1016/j.jcrs.2019.04.004.

[49] J.A. Weiss, B.N. Maker, S. Govindjee, Finite element implementation of incompressible, transversely isotropic hyperelasticity, Comput. Methods Appl. Mech. Eng. 135 (1996) 107–128. https://doi.org/10.1016/0045-7825(96)01035-3.

[50] Y.C. Fung, Biomechanics: Mechanical properties of living tissues, 2nd ed., Springer, New York, 1993.

[51] Y. Song, R.E. Debski, V. Musahl, M. Thomas, S.L.Y. Woo, A three-dimensional finite element model of the human anterior cruciate ligament: a computational analysis with experimental validation, J Biomech. 37 (2004) 383–390.

[52] M. Freutel, F. Galbusera, A. Ignatius, L. Durselen, Material properties of individual menisci and their attachments obtained through inverse FE-analysis, J. Biomech. 48 (2015) 1343–1349. https://doi.org/10.1016/j.jbiomech.2015.03.014.

[53] R. Magalhães, A. Elsheikh, P. Büchler, C. Whitford, J. Wang, Application of particle swarm optimization in inverse finite element modeling to determine the cornea´s mechanical behavior, Acta Sci. - Technol. (2017) 325–331. https://doi.org/10.4025/actascitechnol.v39i3.29884.

[54] R. Magalhães, A. Elsheikh, P. Büchler, C. Whitford, J. Wang, Application of particle swarm optimization in inverse finite element modeling to determine the cornea´s mechanical behavior, Acta Sci. - Technol. (2017). https://doi.org/10.4025/actascitechnol.v39i3.29884.

[55] J. Resende, M.T.C. Faria, E. Barbosa, J. Saffar, Experimental stress-strain curves for the knee cruciate ligaments, in: Proc. COBEM, Brasília, DF, 2007. https://www.researchgate.net/publication/294889432_EXPERIMENTAL_STRESS-STRAIN_CURVES_FOR_THE_KNEE_CRUCIATE_LIGAMENTS (accessed May 21, 2020).

[56] W. Petersen, B. Tillmann, Structure and vascularization of the cruciate ligaments of the human knee joint, Anat Embryol Berl. 200 (1999) 325–334.

[57] P. Kannus, Structure of the tendon connective tissue, Scand. J. Med. Sci. Sports. 10 (2000) 312–320.

[58] M. Benjamin, J.R. Ralphs, Fibrocartilage in tendons and ligaments: An adaptation to compressive load, J. Anat. 193 (1998) 481–494. https://doi.org/10.1046/j.1469-7580.1998.19340481.x.

[59] S.L. Evans, C.A. Holt, H. Ozturk, K. Saidi, N.G. Shrive, Measuring soft tissue properties using digital image correlation and finite element modelling, in: E.E. Gdoutos (Ed.), Exp. Anal. Nano Eng. Mater. Struct., Springer, Dordrecht, 2007: pp. 313–314.

[60] R.M. Castile, N.W. Skelley, B. Babaei, R.H. Brophy, S.P. Lake, Microstructural properties and mechanics vary between bundles of the human anterior cruciate ligament during stress-relaxation, J Biomech. 49 (2016) 87–93. https://doi.org/10.1016/j.jbiomech.2015.11.016.

[61] A. Race, A.A. Amis, The mechanical properties of the two bundles of the human posterior cruciate ligament, J. Biomech. 27 (1994) 13–24. https://doi.org/10.1016/0021-9290(94)90028-0.

[62] D.L. Butler, Y. Guan, M.D. Kay, J.F. Cummings, S.M. Feder, M.S. Levy, Location-dependent variations in the material properties of the anterior cruciate ligament, J. Biomech. 25 (1992) 511–518. https://doi.org/10.1016/0021-9290(92)90091-E.

[63] S.L.Y. Woo, J.M. Hollis, D.J. Adams, R.M. Lyon, S. Takai, Tensile properties of the human femur-anterior cruciate ligament-tibia complex. The effects of specimen age and orientation, Am. J. Sports Med. 19 (1991) 217–225.

[64] S.L.Y. Woo, M.A. Gomez, W.H. Akeson, The time and history-dependent viscoelastic properties of the canine medical collateral ligament, J. Biomech. Eng. 103 (1981) 293–298.

[65] T.A.L. Wren, S.A. Yerby, G.S. Beaupré, D.R. Carter, Mechanical properties of the human achilles tendon, Clin. Biomech. (2001). https://doi.org/10.1016/S0268-0033(00)00089-9.

[66] D.L. Butler, E.S. Grood, F.R. Noyes, R.F. Zernicke, K. Brackett, Effects of structure and strain measurement technique on the material properties of young human tendons and fascia, J. Biomech. (1984). https://doi.org/10.1016/0021-9290(84)90090-3.

[67] T.J. Bonner, N. Newell, A. Karunaratne, A.D. Pullen, A.A. Amis, M.J.B. A, S.D. Masouros, Strain-rate sensitivity of the lateral collateral ligament of the knee, J. Mech. Behav. Biomed. Mater. 41 (2015) 261–270.

[68] J.G. Whitehair, P.B. Vasseur, N.H. Willits, Epidemiology of cranial cruciate ligament rupture in dogs, J. Am. Vet. Med. Assoc. 203 (1993) 1016–1019.

[69] J.P. van der List, D.N. Mintz, G.S. DiFelice, The location of anterior cruciate ligament tears: a prevalence study using magnetic resonance imaging, Orthop. J. Sports Med. 5 (2017). https://doi.org/10.1177/2325967117709966.

Figure Caption (s)

Figure Legends

Fig. 1. (a) Anterior and (b) posterior views of an anterior cruciate ligament. (c) The ligament with speckle patterns.

Fig. 2. The digital image correlation (DIC) setup for testing an anterior cruciate ligament. (a) Schematic view of the DIC setup around the tensile testing machine. (b) Complete built of the DIC setup showing all six cameras, stainless-steel tank and the specimen submerged in 20 ml buffer solution (15ml of 20mM Tris pH 7.5, 150 mM NaCl, 5 mM $CaCl_2$) with protease inhibitors (1 tablet of mini-cOmplete per 10 ml of buffer, SIGMA-ALDRICH/Roche, USA).

Fig. 3. Representative average load-displacement curves at different regions across the surface of the anterior cruciate ligament during a tensile test. Curves for the top, middle (mid) and lower regions obtained from the image correlations using 3D digital image correlation setup and the tensile test on the material testing machine curve obtained from the moving crosshead of the material testing machine. The error bars represent specimen variations (n=5), the maximum

Fig. 4. Total displacement and true strain across the surface of an ACL at maximum load from all three camera pairs. Additional images showing load-displacement distribution can be found in Supplementary Material (Supplementary Materials Fig. S4).

Fig. 5. Schematics showing the process of mapping the three surfaces of the reference object (red, green and blue) on the virtual surface in order to obtain transformation parameters for the 3D digital image correlation test setup. Subsequently, the parameters were applied on to the 3D surfaces of the ligaments to construct 3D point clouds, which were then converted to tight mesh, solid geometry and finally continuous solid finite element models.

Fig. 6. Finite element models of an ACL with hyperelastic material properties showing (a) von Mises stress (S, Mises) and (b) maximum principal logarithmic strain (LE, Max, Principal) across the surface at different views.

Fig. 7. The box plot shows nominal stress and strain calculated from the Ogden material model parameters for the current study. The scattered dots in magenta, blue and red are nominal stress and strain values obtained from previous literature. Although sample deviations appear to be large, the median nominal stresses (the line in the middle of the boxes) agree with the values in the literature.

Figure(s)

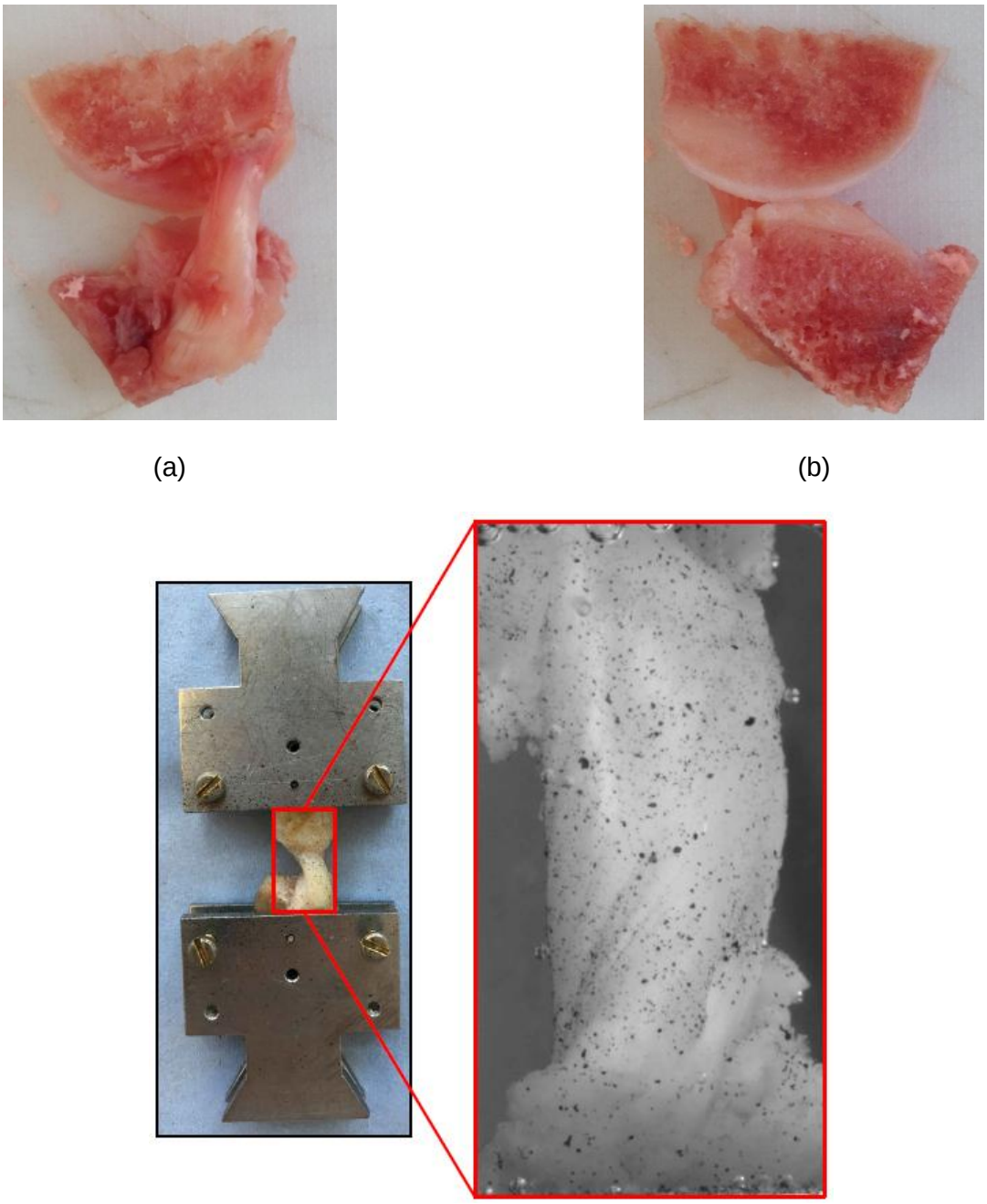

(a) (b)

(c)

Fig. 1. (a) Anterior and (b) posterior views of an anterior cruciate ligament. (c) The ligament with speckle patterns.

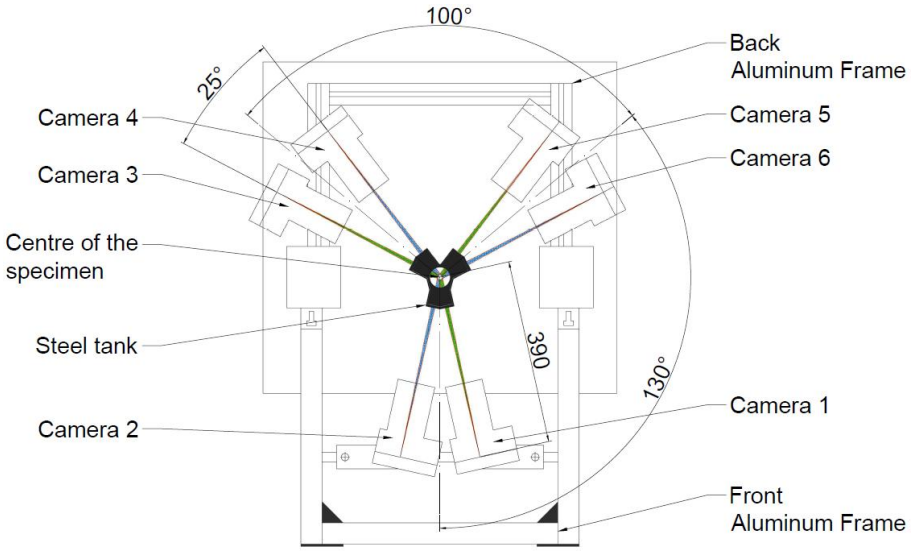

(a)

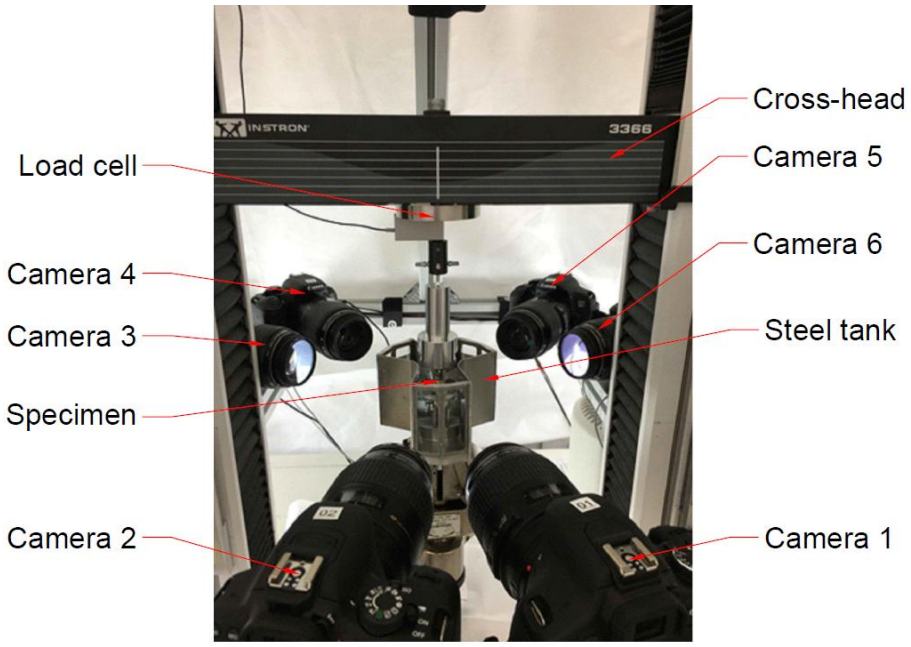

(b)

Fig. 2. The digital image correlation (DIC) setup for testing an anterior cruciate ligament. (a) Schematic view of the DIC setup around the tensile testing machine. (b) Complete built of the DIC setup showing all six cameras, stainless-steel tank and the specimen submerged in 20 ml buffer solution (15ml of 20mM Tris pH 7.5, 150 mM NaCl, 5 mM $CaCl_2$) with protease inhibitors (1 tablet of mini-cOmplete per 10 ml of buffer, SIGMA-ALDRICH/Roche, USA).

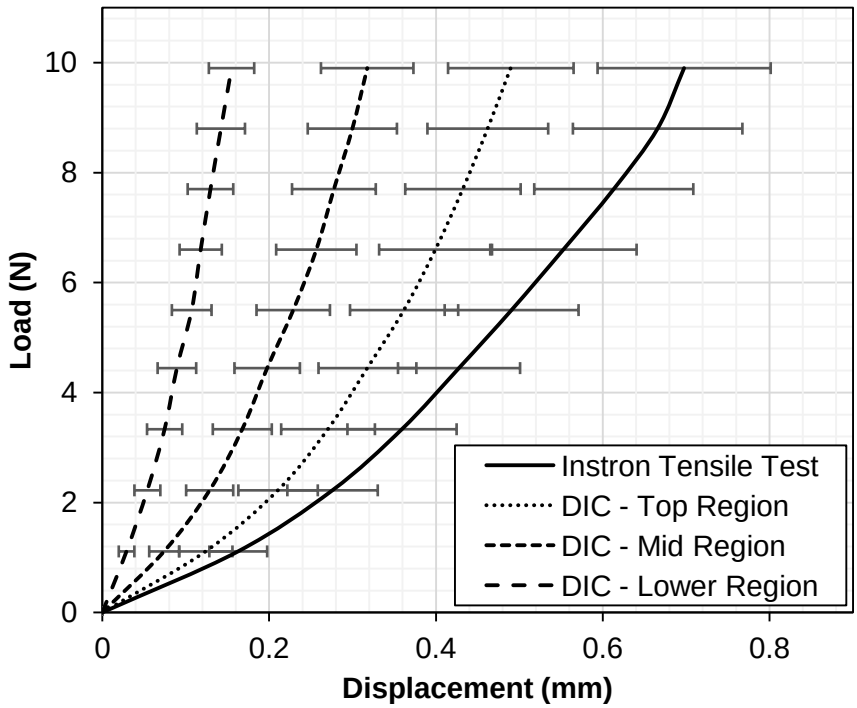

Fig. 3. Representative average load-displacement curves at different regions across the surface of the anterior cruciate ligament during a tensile test. Curves for the top, middle (mid) and lower regions obtained from the image correlations using 3D digital image correlation setup and the tensile test on the material testing machine curve obtained from the moving crosshead of the material testing machine. The error bars represent specimen variations (n=5), the maximum

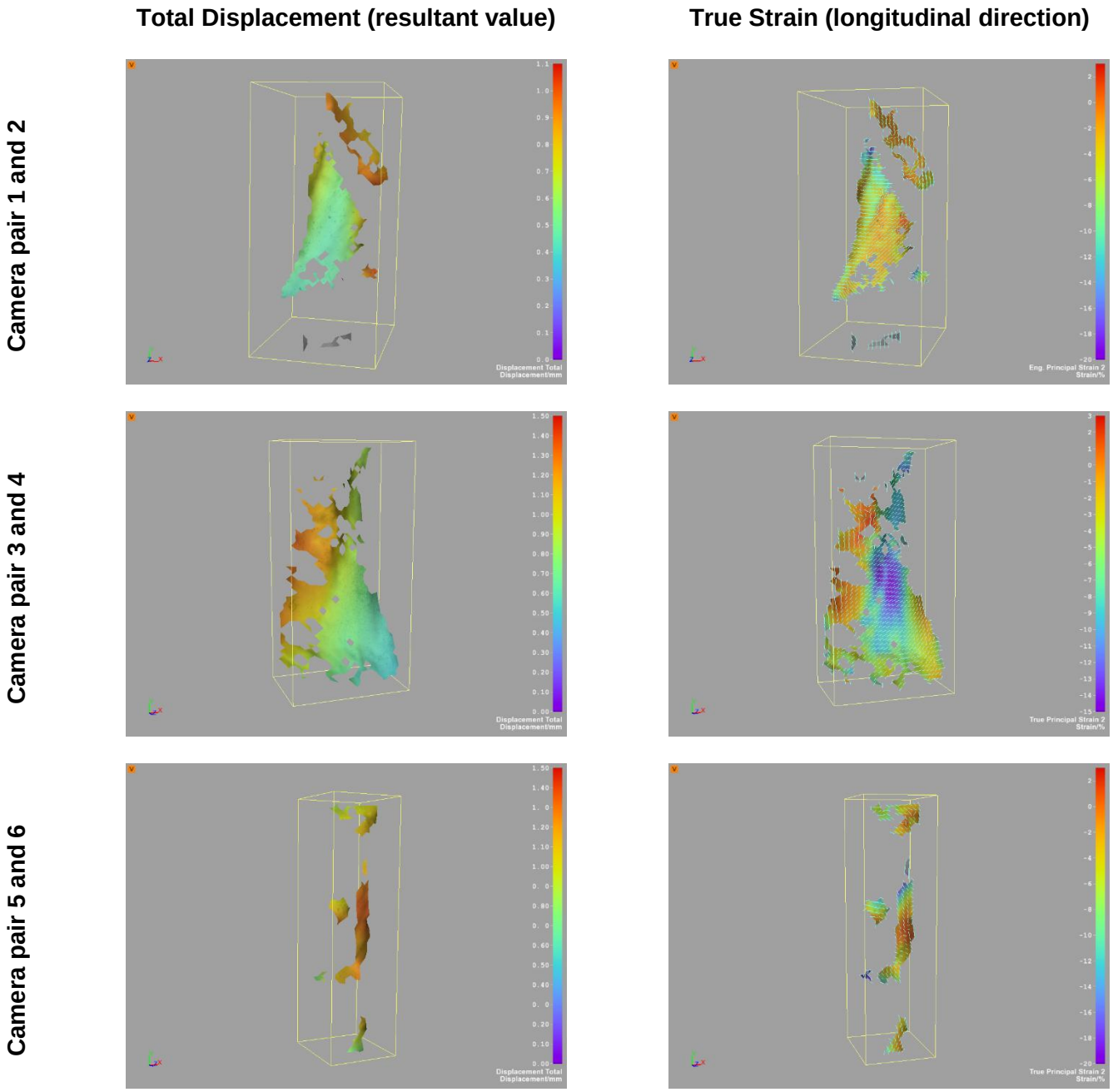

Fig. 4. Total displacement and true strain across the surface of an ACL at maximum load from all three camera pairs. Additional images showing load-displacement distribution can be found in Supplementary Material (Supplementary Materials Fig. S4).

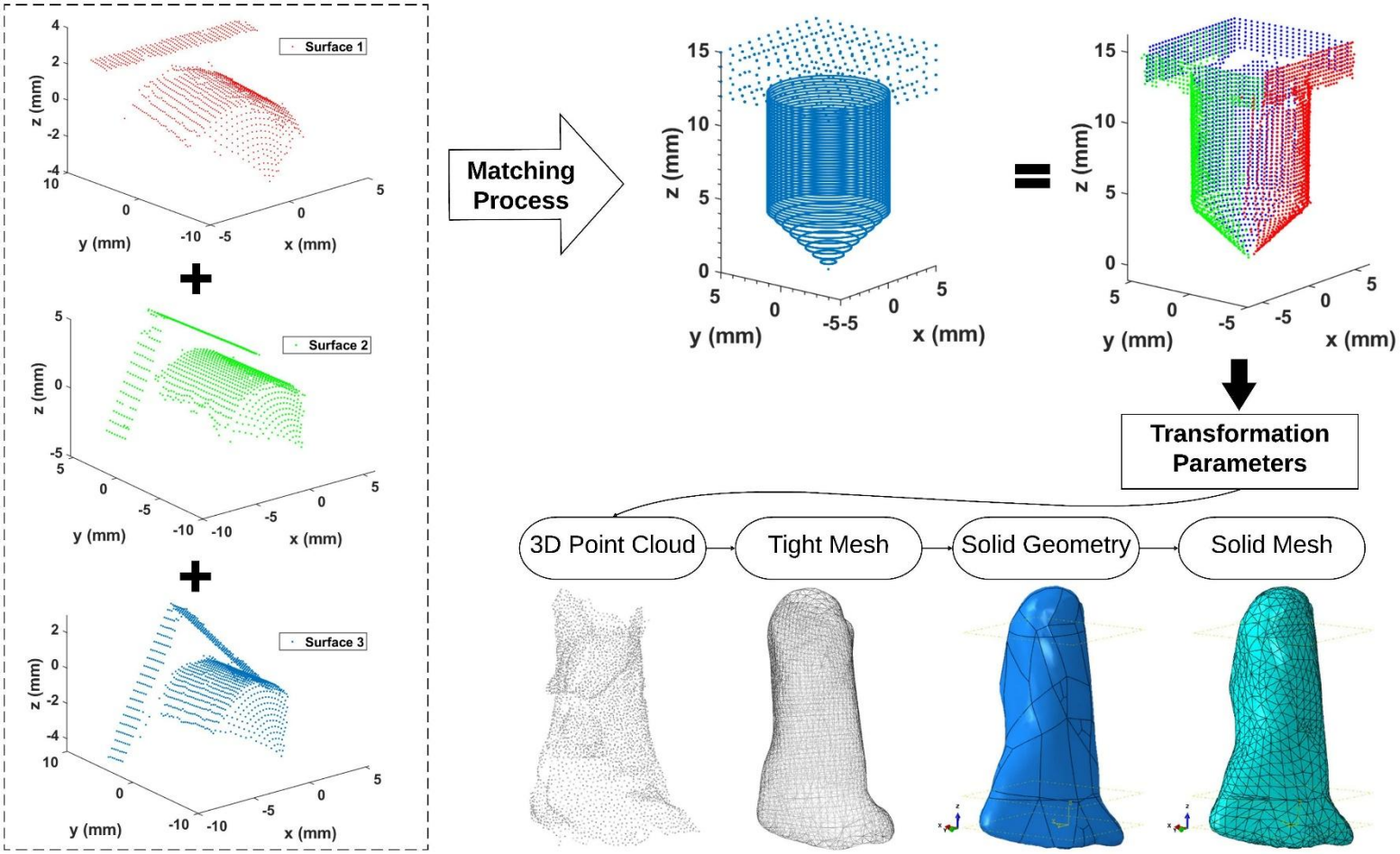

Fig. 5. Schematics showing the process of mapping the three surfaces of the reference object (red, green and blue) on the virtual surface in order to obtain transformation parameters for the 3D digital image correlation test setup. Subsequently, the parameters were applied on to the 3D surfaces of the ligaments to construct 3D point clouds, which were then converted to tight mesh, solid geometry and finally continuous solid finite element models.

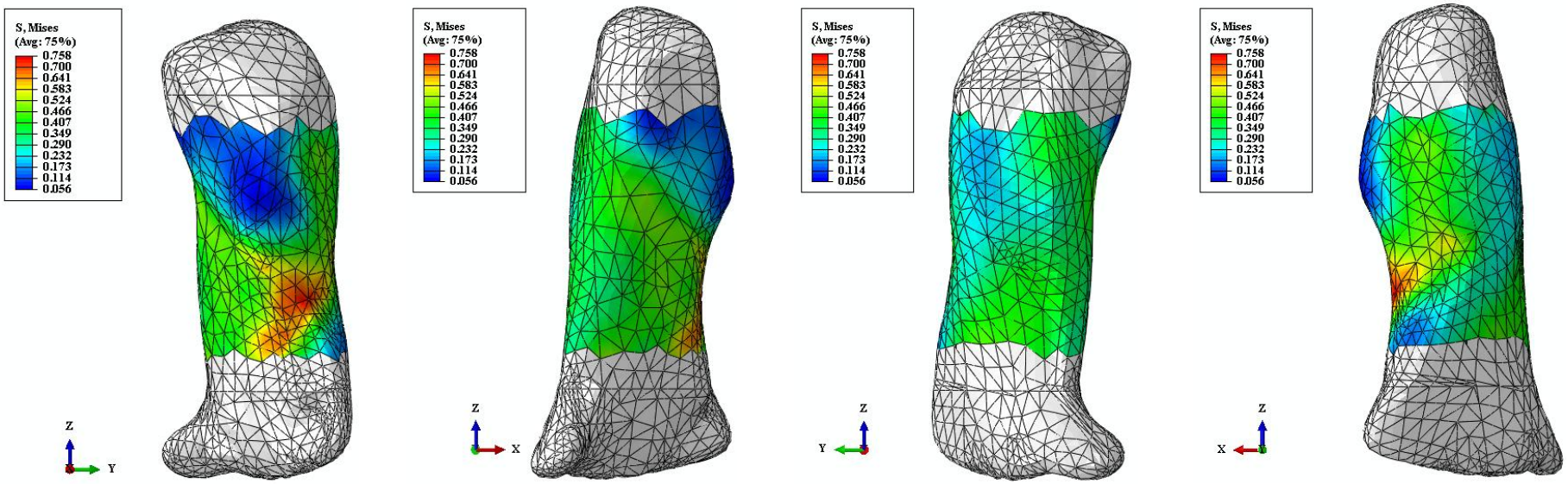
S, Mises
(Avg: 75%)
0.758
0.700
0.641
0.583
0.524
0.466
0.407
0.349
0.290
0.232
0.173
0.114
0.056
Z
Y
X

(a)

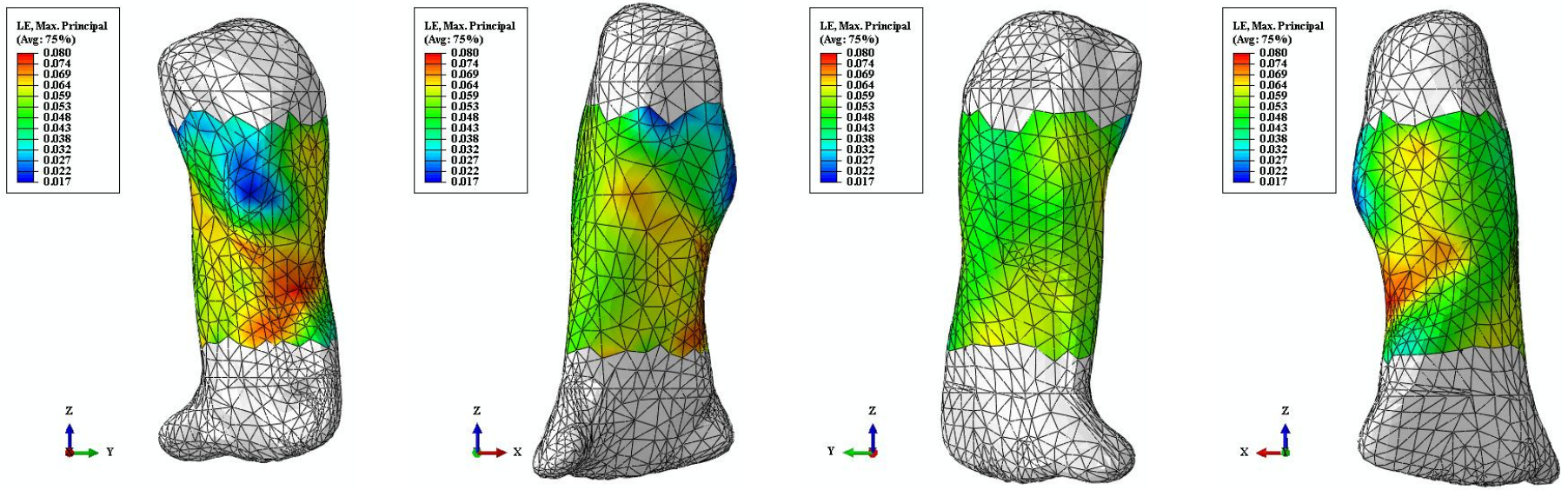
LE, Max. Principal
(Avg: 75%)
0.080
0.074
0.069
0.064
0.059
0.053
0.048
0.043
0.038
0.032
0.027
0.022
0.017
Z
Y
X

(b)

Fig. 6. Finite element models of an ACL with hyperelastic material properties showing (a) von Mises stress (S, Mises) and (b) maximum principal logarithmic strain (LE, Max, Principal) across the surface at different views.

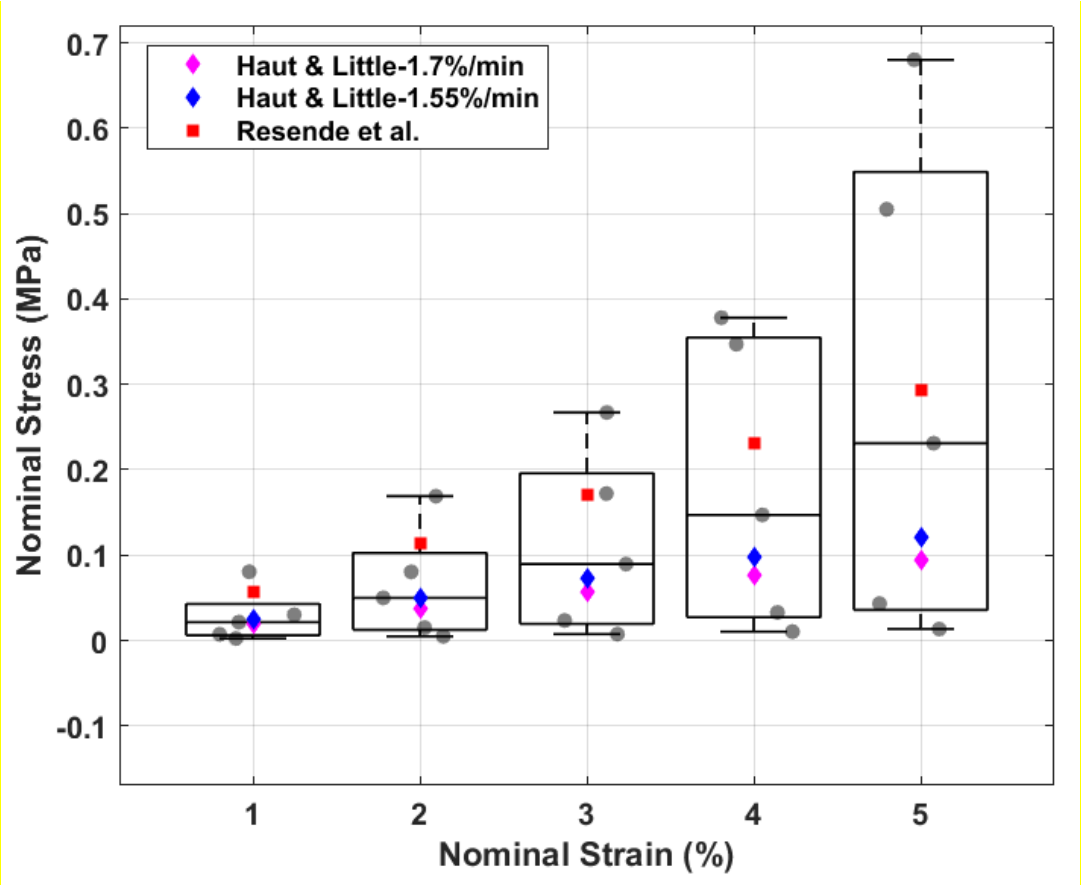

Fig. 7. The box plot shows nominal stress and strain calculated from the Ogden material model parameters for the current study. The scattered dots in magenta, blue and red are nominal stress and strain values obtained from previous literature. Although sample deviations appear to be large, the median nominal stresses (the line in the middle of the boxes) agree with the values in the literature.

Table 1

Numerical parameters (μ and α) derived from inverse analysis of the ACL-specific finite element models defining non-linear hyperelastic characteristics of the ACLs. Root mean square (RMS) values represents the accuracy achieved between experimental and numerical data during the inverse analysis. There are two suspected outliers, and they are μ for specimen one and α for specimen three. The coefficient of variation for both parameters might have been affected because of the suspected outliers.

Specimen No.	μ	α	RMS (%)
1	2.58	20.36	0. 63
2	0.23	17.72	1.11
3	0.82	70.32	0.53
4	0.64	44.52	0.67
5	0.08	14.31	0.76
First Quartile (25%)	0.16	16.01	
Third Quartile (75%)	1.70	57.42	
Interquartile Range (IQR)	1.54	41.40	
Suspected Outliers (Inner Fence: 1.5 x IQR)	2.32	62.11	
Outlier (Outer Fence: 3 x IQR above third quartile)	6.33	181.63	
Outlier (Outer Fence: 3 x IQR below first quartile)	4.48	108.20	
Mean	0.87	33.44	
Standard Deviation	1.00	23.81	
Coefficient of Variation (%)	115.24	71.18	
Mean – excluding outlier	0.44	24.23	
Standard Deviation – excluding outlier	0.34	13.75	
Coefficient of Variation – excluding outlier	78.05	56.77	

Table 2

Longitudinal displacement obtained from the digital image correlation test setup, their corresponding standard deviation, and the coefficient of variation values across the five cadaveric specimens. The highest standard deviation is 54% of the mean and this value decreases with increasing the load with the lowest value being 39%.

Load (N)	Longitudinal Displacement (mm)	Standard Deviation	Coefficient of Variation (%)
0.0	0	0	N/A
1.1	0.074	0.040	54
2.2	0.129	0.063	49
3.3	0.168	0.079	47
4.4	0.198	0.088	44
5.5	0.229	0.099	43
6.6	0.257	0.108	41
7.7	0.278	0.112	40
8.8	0.300	0.120	39
9.9	0.318	0.124	39

Table 3

Longitudinal displacement obtained from the digital image correlation test setup, their corresponding standard deviation, and the coefficient of variation values within the specimens. The standard deviation describes variability of data obtained from different camera pairs. Abbreviations: Dis, longitudinal displacement; SD, standard deviation of the mean; CV, coefficient of variation.

Load (N)	Specimen 1			Specimen 2			Specimen 3			Specimen 4			Specimen 5		
	Dis (mm)	SD	CV (%)	Dis (mm)	SD	CV (%)	Dis (mm)	SD	CV (%)	Dis (mm)	SD	CV (%)	Dis (mm)	SD	CV (%)
0.0	0.000	0.000	N/A	0.000	0.000	N/A	0.000	0.000	N/A	0.000	0.000	N/A	0.000	0.000	N/A
1.1	0.028	0.010	36	0.086	0.047	55	0.036	0.025	69	0.116	0.048	41	0.105	0.024	22
2.2	0.061	0.020	32	0.141	0.073	51	0.065	0.043	66	0.193	0.082	42	0.183	0.042	22
3.3	0.085	0.027	32	0.179	0.089	49	0.087	0.058	66	0.246	0.110	44	0.241	0.059	24
4.4	0.110	0.033	30	0.209	0.101	48	0.105	0.069	66	0.279	0.127	45	0.285	0.073	25
5.5	0.134	0.039	29	0.243	0.109	44	0.121	0.080	65	0.312	0.145	46	0.334	0.088	26
6.6	0.158	0.043	26	0.269	0.113	41	0.136	0.089	65	0.341	0.162	47	0.378	0.086	22
7.7	0.178	0.048	27	0.292	0.117	40	0.149	0.098	65	0.364	0.176	48	0.406	0.099	24
8.8	0.197	0.051	25	0.314	0.122	38	0.161	0.105	65	0.387	0.192	49	0.440	0.100	22
9.9	0.214	0.055	25	0.330	0.132	39	0.172	0.110	64	0.409	0.206	50	0.463	0.104	22

Supplementary Material

Click here to download Supplementary Material: RR_Supplementary Materials_S2.docx

***Declaration of Interest Statement**

Declaration of interests

☒ The authors declare that they have no known competing financial interests or personal relationships that could have appeared to influence the work reported in this paper.

☐The authors declare the following financial interests/personal relationships which may be considered as potential competing interests: